

Antiferromagnetic Spin Correlations Between Corner-Shared $[\text{FeO}_5]^{7-}$ and $[\text{FeO}_6]^{9-}$ Units, in the Novel Iron-Based Compound: BaYFeO_4

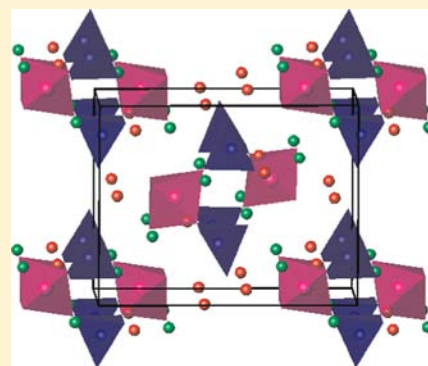
Friederike Wrobel,[†] Moureen C. Kemei,[‡] and Shahab Derakhshan^{*,†}

[†]Department of Chemistry and Biochemistry, California State University, Long Beach, 1250 Bellflower Boulevard, Long Beach, California 90840-3903, United States

[‡]Materials Department and Materials Research Laboratory, University of California, Santa Barbara, California 93106-5121, United States

S Supporting Information

ABSTRACT: A novel quaternary compound in the Ba–Y–Fe–O phase diagram was synthesized by solid-state reaction and its crystal structure was characterized using powder X-ray diffraction. The crystal structure of BaYFeO_4 consists of a unique arrangement of Fe^{3+} magnetic ions, which is based on alternate corner-shared units of $[\text{FeO}_5]^{7-}$ square pyramids and $[\text{FeO}_6]^{9-}$ octahedra. This results in the formation of stairwise channels of FeO polyhedra along the b crystallographic axis. The structure is described in an orthorhombic crystal system in the space group $Pnma$ with lattice parameters $a = 13.14455(1)$ Å, $b = 5.694960(5)$ Å, and $c = 10.247630(9)$ Å. The temperature-dependent magnetic susceptibility data reveal two antiferromagnetic (AFM) transitions at 33 and 48 K. An upturn in the magnetic susceptibility data above these transitions is observed, which does not reach its maximum even at 390 K. The field-dependent magnetization data at both 2 and 300 K show a nearly linear dependence and do not exhibit significant hysteresis. Heat capacity measurements between 2 and 200 K reveal only a broad anomaly without any indication of long-range ordering. The latter data set is not in good agreement with the magnetic susceptibility data, which makes it difficult to exactly determine the magnetic ground state of BaYFeO_4 . Accordingly, a temperature-dependent neutron diffraction study is in order, which will enable resolving this issue. The theoretical study of the relative strengths of magnetic exchange interactions along various possible pathways, using extended Hückel spin dimer analysis, shows that only interactions between square pyramidal and octahedral centers are significant, and among them, the intrachannel correlations are stronger than interchannel interactions. This is the first physical property study in such a magnetic ion substructure.



■ INTRODUCTION

Since the discovery of high-temperature superconductivity in a Ba–La–Cu–O system with a perovskite related structure in 1986, increasing interest in similar materials has started.¹ In an attempt to find materials with higher T_c values, a great deal of effort has been devoted to the synthesis and characterization of novel oxygen deficient perovskites. Among the subsequently discovered related compounds, yttrium barium copper oxide ($\text{YBa}_2\text{Cu}_3\text{O}_7$, YBCO) with mixed-valent copper ions was the first example with a critical temperature above the boiling point of liquid nitrogen, T_c of 93 K.²

Introducing other transition metal ions such as iron to the structure resulted in preparation and investigation of a large number of compounds in this family. In $\text{La}_{0.5}\text{Ba}_{0.5}\text{Fe}_{1-x}\text{Cu}_x\text{O}_{2.75-x/(2+\delta)}$, which was synthesized and characterized by Er-Rakho et al.,³ both iron and copper show mixed valence. The same research group discovered a new yttrium-based compound, $\text{YBaCuFeO}_{5+\delta}$,⁴ which crystallizes in a structure very similar to that of YBCO. Kudryavtsev et al. introduced a series of compounds in the Ln_2O_3 –BaO– $\text{Fe}_2\text{O}_{3+\delta}$

system.⁵ $\text{YBa}_3\text{Fe}_2\text{O}_{7.5+\delta}$ is one of those compounds with an orthorhombic structure, which is isostructural to $\text{YBa}_3\text{Al}_2\text{O}_{7.5}$.⁶ There has also been a strong focus on $\text{YBa}_2\text{Fe}_3\text{O}_{8+w}$ whose structure and properties can be altered by tuning the oxygen content.^{7–9} Another interesting compound, which contains the same elements, is YBaFe_2O_5 . Here, the average oxidation state of iron cations is +2.5 and the material undergoes a Verwey transition at 308 K.^{10,11} All of the above-mentioned compounds belong to the family of oxygen-deficient perovskites. Moreover, in 2008 the iron-based superconductor $\text{La}[\text{O}_{1-x}\text{F}_x]\text{FeAs}$ was discovered.¹² This triggered our current interest in new iron-based compounds.

Here, we report on a novel iron-based compound with the chemical composition of BaYFeO_4 . It is isostructural to a series of platinum-based compounds, namely, $\text{Ba}_2\text{Y}_2\text{CuPtO}_8$, $\text{ErBa}(\text{Cu,Pt})\text{O}_4$, $\text{HoBa}(\text{Cu,Pt})\text{O}_4$, and $\text{Ba}_2\text{Eu}_2\text{ZnPtO}_8$, where the Pt^{4+} ions reside in octahedral (*oct*) voids and divalent transition

Received: January 4, 2012

Published: February 25, 2013

metal ions occupy the square pyramidal (*sp*) positions.^{13–18} This is mainly due to the larger octahedral site preference energies of Pt⁴⁺ ions with low-spin 5d⁶ electronic configuration, which leave the *sp* voids for the Cu²⁺ (or Zn²⁺) ions. Except for Er₂Ba₂CuPtO₈, no physical property measurements were conducted on these compounds. In Er₂Ba₂CuPtO₈, Pt⁴⁺ is diamagnetic and does not effectively contribute to the magnetic properties. However, Er³⁺ ions are coupled antiferromagnetically in the *ac* plane with a small spin-flipping field below 7 K, and the Cu²⁺ ions are correlated antiferromagnetically along the *b* axis below 60 K. The two AFM interactions were proposed to be independent of each other.¹⁸ In the context of magnetic ion arrangement in this crystal structure type, BaYFeO₄ is unique, as it is the first example where both *oct* and *sp* sites are occupied by magnetically active ions, Fe³⁺.

In this paper, the synthesis, crystal structure, and magnetic properties of BaYFeO₄ along with the relative strengths of AFM exchange interactions, which were estimated through theoretical calculations using the extended Hückel tight-binding spin dimer analysis, are presented.

EXPERIMENTAL SECTION

Synthesis. BaYFeO₄ was synthesized using stoichiometric amounts of BaCO₃ (Alfa Aesar, 99.95%), Y₂O₃ (Alfa Aesar, 99.99%), and Fe₂O₃ (Alfa Aesar, 99.99%) as starting materials. Y₂O₃ was dried at 1000 °C for 10 h before weighing. The reactants were weighed, thoroughly ground, and pressed into a pellet in an argon-filled glovebox. The pellet was then placed on a piece of platinum foil in an alumina crucible and preheated at 900 °C for 48 h in air. The sample was reground and pressed into another pellet, which was then heated for 48 h at 1250 °C. The heating rate was 100 °C/h and the cooling rate was 200 °C/h. The process was repeated several times until a nearly phase-pure sample was obtained. All reactions were conducted in air.

Powder X-ray Diffraction. The progress of the reaction and the purity of the sample were monitored via powder X-ray diffraction by a PANalytical X'Pert Pro MPD diffractometer, equipped with a linear X'Celerator detector, with Cu Kα₁ radiation. The X-ray diffraction data were collected at room temperature in the range of 10° ≤ 2θ ≤ 100° with ~0.008° steps. Ambient temperature high-resolution synchrotron X-ray diffraction data were collected at the 11BM beamline at the Advanced Photon Source (APS) at the Argonne National Laboratory. The data collection was performed at 295 K in the angle range 2° ≤ 2θ ≤ 40° at a step of 0.001° using the wavelength of 0.4132(1) Å. The obtained patterns were compared with those of Ba₂Y₂CuPtO₈¹³ and those of other possible competing phases in Ba–Y–Fe–O phase diagram.

Rietveld Refinement. Synchrotron X-ray diffraction data were analyzed by the Rietveld method. The crystal structure was refined based on structural information from the isostructural compound, Ba₂Y₂CuPtO₈¹⁴ as initial model. The General Structure Analysis System (GSAS) suite of programs was employed for this purpose.^{19,20} A pseudo-Voigt peak shape profile, which is a combination of Gaussian and Lorentzian functions, was chosen and the parameters were refined to obtain the best fit to the experimental data.

Physical Property Measurements. Magnetic susceptibility data were collected on a polycrystalline powder sample of BaYFeO₄ encased in a gelatin capsule using a Quantum Design MPMS SQUID magnetometer. Zero-field cooled (ZFC) and field cooled (FC) data were collected over the temperature range 4–390 K under 10 000 and 1000 Oe applied fields. Isothermal field-dependent magnetization measurements were performed at 2 and 300 K in the field range of ±50 000 Oe.

Heat capacity data sets were collected using the Quantum Design Physical Property Measurement System in the temperature range of 4–200 K. Pellets of 50% mass silver and 50% mass sample were cold-pressed for specific heat measurements. Silver was used to increase mechanical strength and to improve thermal contact between the

sample and the stage. Apiezon N grease was employed for further improvement of thermal contact between the stage and the sample. Specific heat contributions of silver and the Apiezon N grease were collected separately and deducted from the total heat capacity to obtain the sample's specific heat.

Computational Methods. The extended Hückel, spin dimer analysis was performed in order to estimate the relative values of the various spin exchange constants *J*.²¹ The intersite hopping energy ⟨Δ*ε*⟩ values were calculated for various dimers ([Fe₂O₁₀]¹⁴⁻, [Fe₂O₁₁]¹⁶⁻, and [Fe₂O₁₂]¹⁸⁻) with the CAESAR and SAMOA packages.^{22,23} For oxygen *s* and *p* states and iron *d* states, double-ζ Slater-type orbitals (STOs), and for the iron *s* and *p* states, single-ζ STOs were used. The values for the valence shell ionization potentials (VSIPs) *H_{ii}* and ζ_{*i*}, and ζ'_{*i*} coefficients are presented in Table 1.

Table 1. ζ_{*i*} and *H_{ii}* Values of the Slater-type Orbitals (STOs)

atom	orbital	<i>H_{ii}</i> [eV]	ζ _{<i>i</i>}	<i>C</i>	ζ' _{<i>i</i>}	<i>C'</i>
O	2s	−32.3	2.688	0.67394	1.675	0.35669
O	2p	−14.8	3.694	0.33219	1.659	0.74478
Fe	4s	−9.1	1.925	1		
Fe	4p	−5.32	1.39	1		
Fe	3d	−12.6	6.068	0.40382	2.618	0.71983

RESULTS AND DISCUSSION

Synthesis and Phase Analyses. The phase diagram of BaO–Y₂O₃–Fe₂O₃ is very rich, making it difficult to prepare a single-phase target compound. Our preliminary X-ray diffraction analyses showed the formation of a phase similar to Ba₂Y₂PtCuO₈ in addition to a trace amount of YFeO₃.

The preparation of the BaYFeO₄ sample was later optimized through addition of trace amount (~3 mol % in total) of BaO in various heating cycles, which resulted in elimination of YFeO₃. The improved sample still contained an unidentified minor impurity phase with rather broad peaks and maximum relative intensity of less than 1% in synchrotron X-ray data (Figure 1b). Crystal structure study and physical property measurements, described in this paper, were performed on the latter sample. Attempts to fit the unidentified peaks to additional structural models from reactants such as Y₂O₃ and BaCO₃ were unsuccessful and did not result in improvement of fitting parameters.

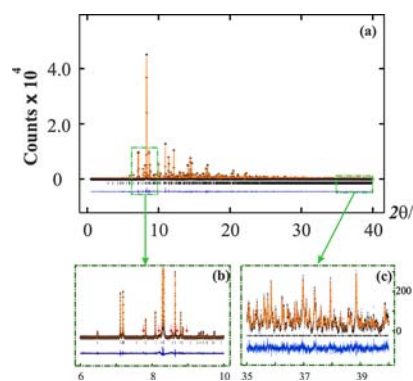


Figure 1. (a) Room-temperature synchrotron powder X-ray diffraction pattern of BaYFeO₄. The crosses indicate the experimental data, while the Rietveld refinement fit to the *Pnma* structure is shown in the solid orange line. The bottom curve shown in the thin blue line gives the difference. (b) Main peaks from unidentified minor side-product are shown by the red arrows. (c) Good agreement between high-quality data and the structural model in the high angle region.

Crystal Structure. BaYFeO₄ crystallizes in the orthorhombic *Pnma* space group. All cations are found in layers with $y = \pm 0.25$. The oxygen ions lie within or between the metal layers. The thermal displacement factors for oxygen were fixed at a reasonable level and were not refined. The powder X-ray diffraction pattern and the Rietveld refinement fit to the structural model are shown in Figure 1a. The cell constants and the refinement parameters are presented in Table 2. The atomic positions as well as the isotropic thermal displacement factors are summarized in Table 3.

Table 2. Rietveld Refinement Results for BaYFeO₄

Empirical formula	BaYFeO ₄
Space group	<i>Pnma</i> (#62)
Lattice parameters	$a = 13.14455(1) \text{ \AA}$ $b = 5.694960(5) \text{ \AA}$ $c = 10.247630(9) \text{ \AA}$ $V = 767.114(1) \text{ \AA}^3$
Z	8
Number of refined parameters	46
Agreement factors	$wRp = 0.0945$ $Rp = 0.0663$

The crystal structure of BaYFeO₄ is presented in Figure 2a. The structure is composed of alternate corner-shared [FeO₅]⁷⁻ square pyramids and [FeO₆]⁹⁻ octahedra, which form four-membered [Fe₄O₁₈]²⁴⁻ rings (Figure 2b). The rings, in turn, are fused via their edges in a perpendicular orientation, which form an infinite [Fe₄O₁₆]²⁰⁻ stairwise arrangement. The Fe³⁺ sublattice with staircase arrangement is presented in Figure 7b. The view from the *ac* crystallographic plane resembles channels, which are extended along the *b* crystallographic axis. Ba1 is coordinated by 11 oxygen ions, while Ba2 is surrounded by 12 oxygen ions, which form a strongly distorted cuboctahedron. Both yttrium atoms are located in monocapped trigonal prismatic coordination environments. The [YO₇]¹¹⁻ units share their edges. Some selected M–O distances are summarized in Table 4.

The calculated bond valence sums (BVS)²⁴ for all the cations are summarized in Table 5. It is noteworthy to mention that the BVS for Fe2 is 2.701, which is lower than what is expected for Fe³⁺. Although the average interionic distances in the octahedral environment of Fe2 are slightly larger than typical Fe³⁺–O²⁻ distances, the presence of iron with lower oxidation state in this reaction condition is not very likely. This can be explained by the weakness of X-ray diffraction methods in

determination of the precise location of light atoms such as oxygen.

Magnetic Properties. ZFC and FC magnetic susceptibility data show the presence of two rather sharp maxima at 33 and 48 K (Figure 3). A broad feature is observed at around 12 K in the ZFC measurement under a 1000 Oe field, which is suppressed in a 10 000 Oe field. Subsequent analysis of temperature-dependent susceptibility data is performed on the 10 000 Oe ZFC and FC curves. There is an upturn in the susceptibility above ~200 K, which does not reach its maximum within the experimental temperature range.

Since we did not reach the paramagnetic regime even at 390 K, we were unable to fit the data to the Curie–Weiss equation and deduce parameters such as effective magnetic moment or Weiss constant. The presence of the minimum at ~200 K and the subsequent upturn to 390 K could suggest the presence of high-temperature magnetic ordering, such as low-dimensional AFM, in BaYFeO₄ which would be characterized by a susceptibility maximum for $T > 390 \text{ K}$.

Fisher heat capacity analysis was performed employing the ZFC susceptibility data. For this purpose, $d\chi/dT$ was plotted as a function of temperature (Figure 4).²⁵ Two lambda-shaped anomalies, which occur exactly at the temperatures of the sharp maxima, are suggestive of long-range AFM order.

The magnetization data as a function of the magnetic field at 2 K and 300 K are presented in Figure 5, which show very weak hysteresis at both temperatures and magnetizations on the order of $10^{-3} \mu_B$ indicating that any ferromagnetic (FM) component is very small. These data indicate that AFM exchange interactions are dominant in this temperature range. For the 2 K data, there is a slight convex curvature which might be understood in terms of the behavior of the Brillouin function for ions with large number of unpaired electrons, $S = 5/2$.

Specific Heat. Remarkably, the heat capacity data (Figure 6) reveal only a broad anomaly and do not show any lambda-like anomalies at the susceptibility maxima. This suggests that only little changes in spin entropy occur at the temperatures where the lambda-shaped anomalies in the Fisher heat capacity analysis were observed. Accordingly, the heat capacity data do not support the occurrence of long-range AFM order at these temperatures. The lack of significant change in entropy at 33 and 48 K regions could be explained by the occurrence of strong exchange interactions above 390 K. Our future temperature-dependent neutron diffraction studies as well as high-temperature magnetic susceptibility data collection for this system should provide a better understanding of magnetic ordering in BaYFeO₄.

Table 3. Atomic Coordinates and Displacement Factors for BaYFeO₄ at Room Temperature

Wyckoff	atom	<i>x</i>	<i>y</i>	<i>z</i>	$U_{\text{iso}} [\text{\AA}^2]$
4c	Ba1	0.21160(3)	0.25000	0.67391(4)	0.0091(1)
4c	Ba2	0.41469 (4)	0.25000	0.39585(4)	0.00945(9)
4c	Y1	0.41454(5)	0.25000	0.01515(5)	0.0029(1)
4c	Y2	0.14338(4)	0.25000	0.30916(6)	0.0029(1)
4c	Fe1	0.46938(7)	0.25000	0.71622(9)	0.0028(2)
4c	Fe2	0.18978(8)	0.25000	0.02204(9)	0.0028(2)
4c	O1	0.5819(4)	0.25000	0.6144 (4)	0.015
4c	O2	0.2914(4)	0.25000	0.1822(4)	0.015
8d	O3	0.0049(3)	0.5089(6)	0.3578(3)	0.015
8d	O4	0.2174(2)	0.5088(6)	0.4404(3)	0.015
8d	O5	0.1107(3)	0.998(7)	0.1322(3)	0.015

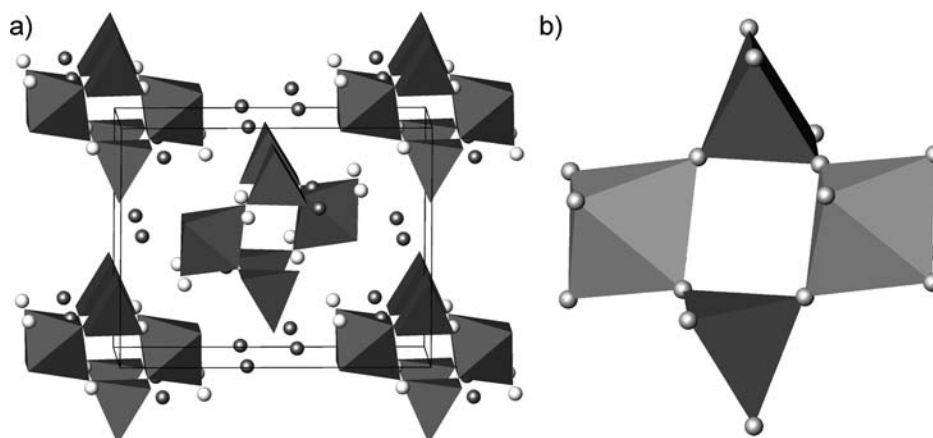


Figure 2. (a) Crystal structure of BaYFeO₄. View along the *b* axis. The lattice is built up from corner-shared [FeO₆]⁷⁻ square pyramids and [FeO₆]⁹⁻ octahedra. Barium and yttrium are shown by light gray and dark gray spheres, respectively. (b) Corner-shared octahedra and square pyramids forming [Fe₄O₁₈]²⁴⁻ rings.

Table 4. Selected Interatomic Distances [Å]

Ba1–O1	2.760(5)	Ba2–O2	2.724(5)
2 × Ba1–O5	2.763(3)	2 × Ba2–O5	2.823(3)
2 × Ba1–O4	2.811(3)	2 × Ba2–O1	2.8498(2)
2 × Ba1–O2	2.8490(2)	2 × Ba2–O5	2.963(4)
2 × Ba1–O3	3.176(3)	2 × Ba2–O4	3.018(3)
2 × Ba1–O4	3.196(3)	Ba2–O1	3.137(5)
		2 × Ba2–O3	3.215(3)
2 × Y1–O3	2.297(3)	2 × Y2–O4	2.220(3)
Y1–O2	2.357(5)	2 × Y2–O5	2.353(3)
2 × Y1–O4	2.341(3)	Y2–O2	2.340(5)
2 × Y1–O3	2.368(3)	2 × Y2–O3	2.395(3)
Fe1–O1	1.810(5)	Fe2–O1	1.991(5)
2 × Fe1–O5	1.960(4)	2 × Fe2–O4	2.019(3)
2 × Fe1–O3	2.026(3)	2 × Fe2–O5	2.101(4)
		Fe2–O2	2.116(5)

Table 5. Calculated Bond Valence Sums for All Six Cationic Positions in BaYFeO₄

	Ba1	Ba2	Y1	Y2	Fe1	Fe2
BVS	2.095	2.064	2.961	3.117	3.005	2.701

Computational Methods. According to the Hubbard model for correlated systems, the magnetic exchange interaction constants, *J* values, are related to the hopping energies, Δe , in a given pathway and the Coulomb constant, U_{eff}

$$J \cong \frac{\langle (\Delta e)^2 \rangle}{U_{\text{eff}}} \quad (1)$$

Since Coulomb constants do not vary with the pathway, one can obtain the relative strengths of different *J* values by calculating the hopping integrals in different dimer units. Employing the extended Hückel method, we calculated the energy levels of the Fe³⁺ 3d orbitals, which contribute to the magnetic interactions. These levels were assigned as pairs (bonding and antibonding) and the gaps between the pairs, $\Delta e_{\mu\mu}$, were calculated. The overall hopping energy for each pathway was calculated by eq 2.

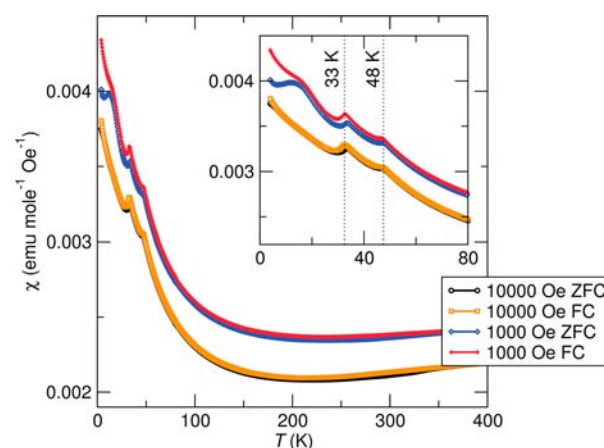


Figure 3. ZFC and FC temperature dependent magnetic susceptibility data of BaYFeO₄ measured under fields of 10 000 and 1000 Oe. The inset shows two maxima at 33 and 48 K. A broad maximum near 12 K, observed in the 1000 Oe ZFC curve, is suppressed under high fields.

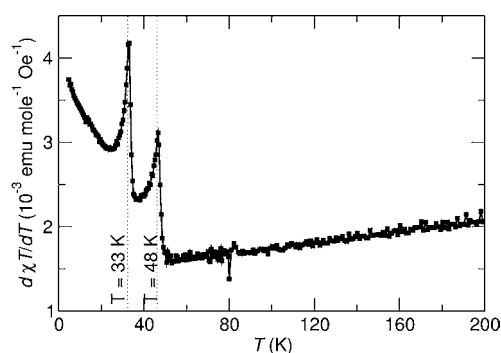


Figure 4. Fisher heat capacity diagram calculated from ZFC data (10 000 Oe).

$$\langle (\Delta e)^2 \rangle \approx \frac{1}{N^2} \sum_{\mu=1}^N (\Delta e_{\mu\mu})^2 \quad (2)$$

All the possible interactions between Fe³⁺ centers were examined revealing that only the interactions between square pyramids and octahedral centers, *sp-oct*, are significant and there is almost no AFM interaction between *oct-oct* and *sp-sp* sites.

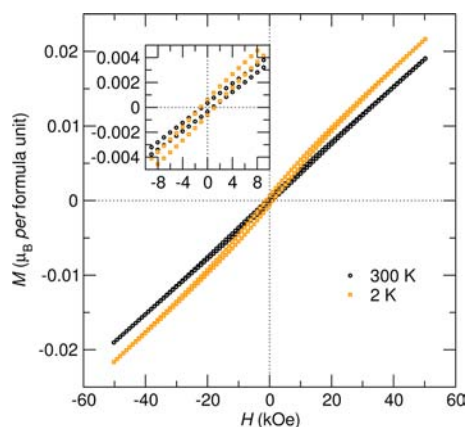


Figure 5. Field-dependent magnetic susceptibility of BaYFeO₄ measured at 2 K and 300 K. The inset illustrates the field-dependent behavior in a higher magnification. The slight curvature in 2 K data is likely due to the Brillouin function behavior for such large $S = 5/2$ and low temperature.

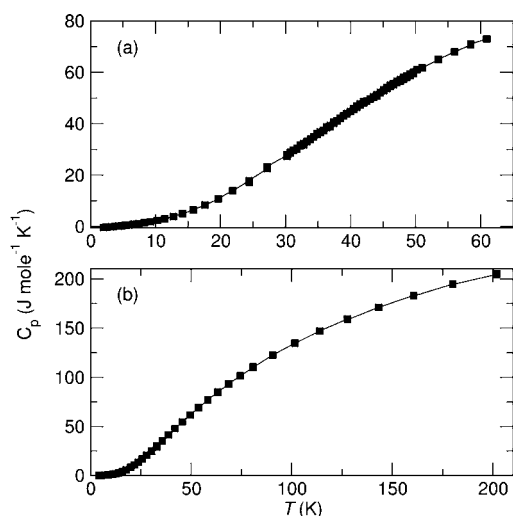


Figure 6. Temperature-dependent heat capacity data. The absence of sharp lambda-shaped peaks indicates an absence of long-range magnetic order in this material. The two data sets, (a) and (b), represent measurements over different temperature ranges for the same sample under zero magnetic field.

Among the *sp-*oct** interactions, four strongest spin exchange pathways are shown in Figure 7a. In Figure 8, orbitals for bonding and the corresponding antibonding interaction are displayed for the J_1 interaction pathway. The most important possible magnetic structures based on the relative strengths of the four significant exchange pathways are summarized in Table 6.

The relative strengths of AFM coupling of these four interactions are presented in Table 7. Two intrachannel interactions (J_1 and J_2) are much stronger than the interchannel interactions (J_3 and J_4). J_3 and J_4 are almost equally strong. J_2 interactions form zigzag chains running along the b direction. Two adjacent chains are interconnected via J_1 interactions. This results in a stairwise arrangement of iron ions, which in turn form channels along the b crystallographic axis. The J_1 interactions make up the front edges of the stair, while the J_2 interactions build up the side edges. In Figure 7b, only these intrachannel interactions are drawn in order to show how these

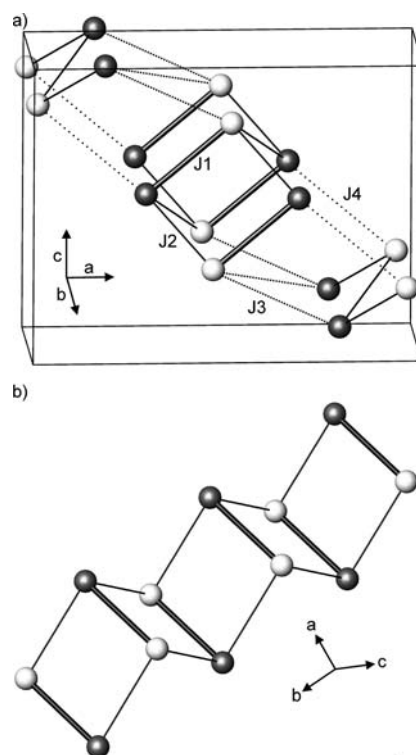


Figure 7. (a) Schematic representation of the four strongest Fe–Fe interactions where J_1 is the strongest, followed by J_2 , J_3 , and J_4 . (b) Schematic representation of the channels, built up by J_1 and J_2 interactions, which resemble a staircase. The unit cell is extended along the b direction. Light-colored Fe³⁺ are in a square pyramidal coordination environment, while dark-colored Fe³⁺ reside in octahedral environments.

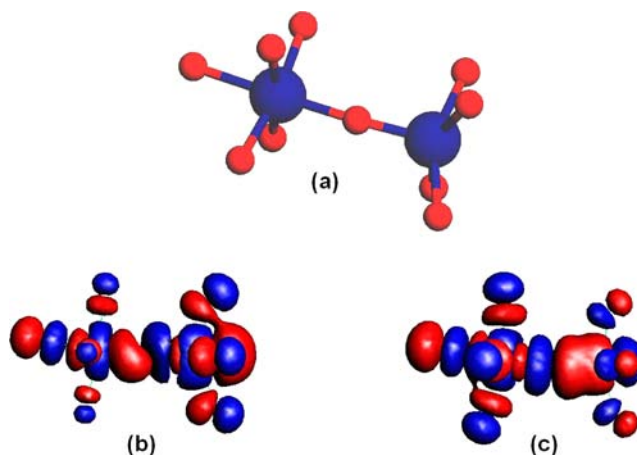


Figure 8. J_1 super exchange interaction between octahedral and square pyramidal sites: (a) *oct-sp* dimer, (b) bonding interaction, (c) antibonding interaction.

Table 6. Different Possible Magnetic Structures Based on the Fe³⁺ Spin Correlations

relative interaction magnitude	model
$J_1 \gg J_2, J_3, \text{ and } J_4$	dimer
$J_2 \gg J_1, J_3, \text{ and } J_4$	zigzag chain
$J_1, \text{ and } J_2 \gg J_3 \text{ and } J_4$	channel
$J_1, J_2, J_3, \text{ and } J_4 \text{ all significant}$	3D structure

Table 7. $\langle(\Delta_e)^2\rangle$ Values and Relative Values for the Four Strongest Exchange Interactions, J_i

	$\langle(\Delta_e)^2\rangle$ [meV ²]	Rel.
J_1	21108	1
J_2	14546	0.69
J_3	8823	0.42
J_4	8678	0.41

interactions could potentially build up one-dimensional magnetic interactions if the J_3 and J_4 interactions were negligible. J_3 and J_4 are responsible for interconnecting the channels and increasing the dimension of the magnetic structure.

Based on this theoretical analysis, it is possible to understand the origin of strong low-dimensional AFM correlations in this material. J_1 and J_2 are the strongest exchange interactions and these are confined to the staircase double chains. Thus, one would expect to find robust quasi-one-dimensional spin correlations in this material. Given that the interstaircase exchanges, J_3 and J_4 , are weaker by only a factor of 2 or so and not by orders of magnitude, it is surprising that there is scant evidence for long-range AFM.

CONCLUSION

A new iron-based compound with the chemical composition of BaYFeO_4 was synthesized. The crystal structure was refined by the Rietveld method from synchrotron powder X-ray data using isostructural $\text{Ba}_2\text{Y}_2\text{CuPtO}_8$ as a model. Temperature-dependent magnetic susceptibility data revealed two anomalies at 33 K and 48 K. The susceptibility data also show a minimum at ~ 200 K followed by an upturn to 390 K which is suggestive of high-temperature magnetic exchange interactions. Isothermal field-dependent magnetization data at both 2 and 300 K are in agreement with dominant AFM behavior for BaYFeO_4 , within the temperature range. The heat capacity data suggest little change in entropy and do not support long-range ordering at the low-temperature magnetic transitions. Theoretical studies based on a spin dimer analysis suggest that the most significant AFM interactions take place between *sp* and *oct* units. AFM correlations within the channels were found to be stronger than those between channels, supporting a low-dimensional model.

Due to the ambiguous nature of the apparent magnetic transitions, we propose neutron diffraction studies to elucidate the magnetic structure. In addition, high-temperature magnetic susceptibility data will be collected to clarify the nature of magnetic interactions at elevated temperatures. If the paramagnetic regime can be reached, the Weiss constant can be determined, which will provide more clarification of the nature of the dominant magnetic exchange interactions.

ASSOCIATED CONTENT

Supporting Information

One powder X-ray crystallographic file (CIF). This material is available free of charge via the Internet at <http://pubs.acs.org>.

AUTHOR INFORMATION

Corresponding Author

*E-mail: shahab.derakhshan@csulb.edu.

Notes

The authors declare no competing financial interest.

ACKNOWLEDGMENTS

We would like to thank Professor John E. Greedan for fruitful discussions and his beneficial comments. We are extremely thankful for the discussions with Professor Ram Seshadri and his comments and support. S.D. is grateful for financial support from the Research Corporation for Science Advancement (Cottrell College Science Award #19761) and the College of Natural Sciences at CSULB for the startup fund. F.W. is thankful for the generous Fulbright grant, which enabled her to study at CSULB. M.C.K. is grateful for the support of the National Science Foundation through the Materials World Network grant (DMR 1105301) and the Schlumberger Foundation Faculty for the Future Fellowship. We acknowledge the use of shared facilities of the Materials Research Laboratory: an NSF MRSEC supported by NSF DMR 1121053. The 11-BM beamline at the Advanced Photon Source is supported by the Department of Energy, Office of Science, Office of Basic Energy Sciences under contract no. DE-AC02-06CH11357.

ABBREVIATIONS:

AFM, antiferromagnetic; FM, ferromagnetic; ZFC, zero field cooled; FC, field cooled; *oct*, octahedral; *sp*, square pyramid; STO, Slater type orbital; BVS, bond valence sums

REFERENCES

- (1) Bednorz, J. G.; Müller, K. A. *Z. Phys. B: Condens. Matter* **1986**, *64*, 189.
- (2) Wu, M. K.; Ashburn, J. R.; Torng, C. J.; Hor, P. H.; Meng, R. L.; Gao, L.; Huang, Z. J.; Wang, Y. Q.; Chu, C. W. *Phys. Rev. Lett.* **1987**, *58*, 908.
- (3) Er-Rakho, L.; Michel, C.; Studer, F.; Raveau, B. *J. Phys. Chem. Solids* **1987**, *48*, 377.
- (4) Er-Rakho, L.; Michel, C.; Lacorre, P.; Raveau, B. *J. Solid State Chem.* **1988**, *73*, 531.
- (5) Kudryavtsev, D. A.; Mill, B. V.; Vedernikov, N. F.; Shaplygin, I. S. *Inorg. Mater.* **1992**, *28*, 943.
- (6) Kovba, L. M.; Lykova, L. N.; Rozova, M. G. *Zh. Neorg. Khim.* **1984**, *29*, 3137.
- (7) Karen, P.; Suard, E.; Fauth, F. *Inorg. Chem.* **2005**, *44*, 8170.
- (8) Karen, P.; Kjekshus, A.; Huang, Q.; Karen, V. L.; Lynn, J. W.; Rosov, N.; Natali Sora, I.; Santoro, A. *J. Solid State Chem.* **2003**, *174*, 87.
- (9) Yuen, T.; Seyedahmadian, M.; Salomon, R. E.; Myer, G. H.; Cao, G. *J. Appl. Phys.* **1996**, *79*, 6001.
- (10) Woodward, P. M.; Karen, P. *Inorg. Chem.* **2003**, *42*, 1121.
- (11) Spiel, C.; Blaha, P.; Karlhein, S. *Phys. Rev. B* **2009**, *79*, 115123.
- (12) Kamihara, Y.; Watanabe, T.; Hirano, M.; Hosono, H. *J. Am. Chem. Soc.* **2008**, *130*.
- (13) Winnea, J. S.; Steinfink, H. *Acta Crystallogr., Sect. C: Cryst. Struct. Commun.* **1987**, *43*, 2436.
- (14) Lalignat, Y.; Ferey, G.; Hervieu, M.; Raveau, B. *Europhys. Lett.* **1987**, *4*, 1023.
- (15) Saito, Y.; Ukei, K.; Shishido, T.; Fukuda, T. *Acta Crystallogr., Sect. C: Cryst. Struct. Commun.* **1990**, *46*, 970.
- (16) Sfreddo, O.; Rabbow, Ch.; Müller-Buschbaum, Hk. *Z. Anorg. Allg. Chem.* **1996**, *622*, 1129.
- (17) Shishido, T.; Fukuda, T.; Toyota, N.; Ukei, K.; Sasaki, T. *J. Cryst. Growth* **1987**, *85*, 599.
- (18) Toyota, N.; van den Beek, C.; Mydosh, J. A.; Koorevaar, P.; van den Berg, J.; Kes, P.; Nishihara, Y.; Murata, K.; Shishido, T.; Saito, Y.; Ukei, K.; Sasaki, T.; Iwasaki, H.; Fukuda, T. *J. Magn. Magn. Mater.* **1990**, *90*, 237.
- (19) Larson, A. C.; Von Dreele, R. B. *General Structure Analysis System (GSAS)*; Los Alamos National Laboratory Report LAUR 2000, p 86.
- (20) Toby, B. H. *J. Appl. Crystallogr.* **2001**, *34*, 210.

- (21) Whangbo, M.-H.; Koo, H.-J.; Dai, D. J. *Solid State Chem.* **2003**, *176*, 417.
- (22) Ren, J.; Liang, W.; Whangbo, M.-H. *Crystal and Electronic Structure Analysis Using CAESAR*, 1998; <http://www.primec.com/>
- (23) Dai, D.; Ren, J.; Liang, W.; Whangbo, M.-H. *Structure And Molecular Orbital Analyzser (SAMOA) program package*; <http://chvamw.chem.ncsu.edu>
- (24) Brown, I. D. *Chem. Soc. Rev.* **1978**, *7*, 359.
- (25) Fisher, M. E. *Philos. Mag.* **1962**, *7*, 1731.